Monthly Notices
of the
ROYAL ASTRONOMICAL SOCIETY

Mon. Not. R. Astron. Soc. **416,** 927–940 (2011) doi:10.1111/j.1365-2966.2011.19082.x

Wide-field optical imaging on ELAIS N1, ELAIS N2, First Look Survey and Lockman Hole: observations and source catalogues

E. A. González-Solares,[1⋆] M. Irwin,[1] R. G. McMahon,[1] S. Hodgkin,[1] J. R. Lewis,[1] N. A. Walton,[1] M. Jarvis,[2] L. Marchetti,[3] S. Oliver,[4] I. Pérez-Fournon,[5] B. Siana,[6] J. Surace[7] and M. Vaccari[3]

[1]*Institute of Astronomy, Madingley Road, Cambridge CB3 0HA*
[2]*Centre for Astrophysics Research, Science & Technology Research Institute, University of Hertfordshire, Hatfield AL10 9AB*
[3]*Dipartimento di Astronomia, Università di Padova, vicolo Osservatorio, 3, 35122 Padova, Italy*
[4]*Astronomy Centre, Department of Physics & Astronomy, University of Sussex, Brighton BN1 9QH*
[5]*Institute de Astrofisica de Canarias, C/ Via Lactea s/n, E-38200 La Laguna, Spain*
[6]*California Institute of Technology, MS 249-17, Pasadena, CA 91125, USA*
[7]*Spitzer Science Center, California Institute of Technology, MC 220-6, 1200 East California Boulevard, Pasadena, CA 91125, USA*

Accepted 2011 May 16. Received 2011 May 11; in original form 2011 March 7

ABSTRACT

We present *u-, g-, r-, i-* and *z*-band optical images and associated catalogues taken primarily with the Isaac Newton Telescope Wide Field Camera on the European Large Area *ISO* Survey (ELAIS) N1 and N2, First Look Survey and Lockman Hole fields comprising a total of 1000 h of integration time over 80 deg^2 and approximately 4.3 million objects. In this paper we outline the observations and data processing and characterize the completeness, reliability, photometric and astrometric accuracy of this data set. All images have been photometrically calibrated using the Sloan Digital Sky Survey and a uniform and homogeneous data set is composed over all the observed fields. Magnitude limits are *u, g, r, i, z* of 23.9, 24.5, 24.0, 23.3, 22.0 (AB, 5σ). These data have been used for optical identification of past and ongoing projects including the surveys ELAIS, *Spitzer* Wide-Area Infrared Extragalactic Survey, *Spitzer* Extragalactic Representative Volume Survey and *Herschel* Multi-tiered Extragalactic Survey.

Key words: techniques: image processing – techniques: photometric – catalogues – surveys – galaxies: photometry – galaxies: statistics.

1 INTRODUCTION

Optical data play a major role in the identification of objects detected at other wavelengths. In particular they are crucial to the characterization process, including morphology classification and photometric redshifts. Telescopes equipped with a large-field mosaic camera have been used to carry out large-area surveys, including SuprimeCam on Subaru (Miyazaki et al. 2002) or Megacam on Canada–France–Hawaii Telescope (Boulade et al. 1998). More recently, and specially with the success of the Sloan Digital Sky Survey (SDSS; York et al. 2000), facilities to image large areas of the sky have been planned or already set up, e.g. the Panoramic Survey Telescope & Rapid Response Systeam (Pan-STARRS; Kaiser et al. 2002), the Large Synoptic Survey Telescope (LSST; Sweeney 2006), SkyMapper (Rakich et al. 2006) and the Very Large Telescope Survey Telescope (VST; Capaccioli, Mancini & Sedmak 2002; Iwert et al. 2006). In the near-infrared (near-IR), and after the Two Micron All Sky Survey (2MASS; Skrutskie et al. 2006), the United Kingdom Infrared Deep Sky Survey (UKIDSS; Lawrence et al. 2007) and the Visible and Infrared Survey Telescope for Astronomy (VISTA; Emerson et al. 2004) are currently producing data with great success. In particular VST and VISTA are two dedicated survey telescopes to carry out the new generation of optical and near-IR public surveys at the European Southern Observatory (Arnaboldi et al. 2007).

The Isaac Newton Telescope (INT) in particular has been successfully used to carry out large projects like the INT Photometric Hα Survey of the Northern Galactic Plane (Drew et al. 2005), the UV-Excess Survey of the Northern Galactic Plane (Groot et al. 2009) and the Wide Field Survey (WFS; McMahon et al. 2001; Irwin et al. 2005).

The data set described here builds upon the WFS data, extending it to a larger coverage (Fig. 1), and has been used in the

⋆E-mail: eglez@ast.cam.ac.uk

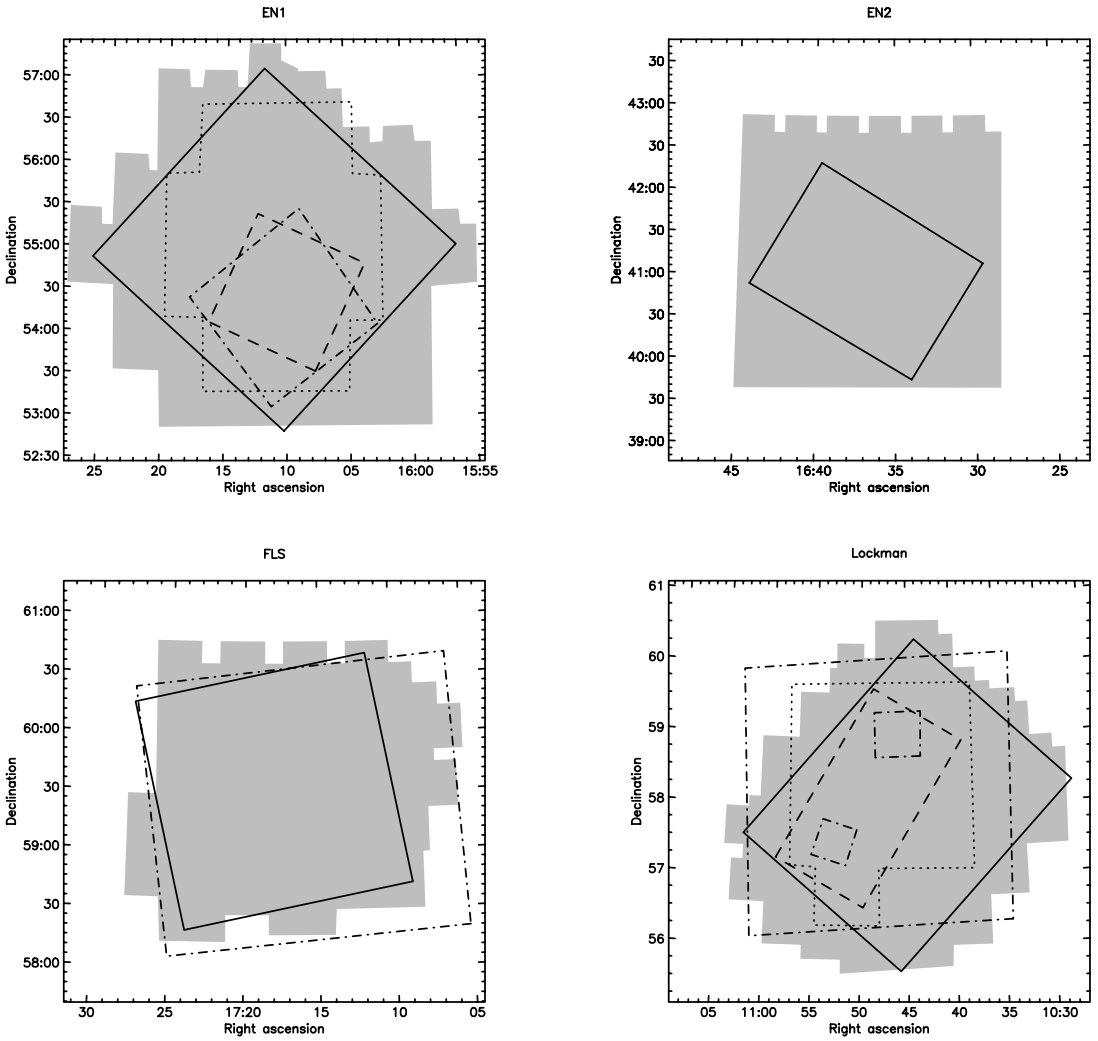

Figure 1. Coverage of the WFC data (grey area). The continuous line shows the *Spitzer* SWIRE coverage, the dashed line the SERVS coverage, the dotted line the UKIDSS coverage and the dot–dashed line the HerMES coverage (not shown are the coverages of EN1 and EN2 which coincide with the SWIRE regions).

identification of sources from the ELAIS *ISO* Survey (Oliver et al. 2000; Rowan-Robinson et al. 2004; Gonzalez-Solares et al. 2005), as well as from the SWIRE *Spitzer* Survey (Lonsdale et al. 2003) and its photometric redshift catalogue (Rowan-Robinson et al. 2008). The first INT Wide Field Camera (WFC) data were originally obtained as part of the WFS and the area covered has been progressively incremented to a larger coverage and additional areas by further observations in subsequent observing periods as described below. These data are being used for the identification of objects and photometric redshifts in the more recent UKIDSS Deep Extragalactic Survey (DXS), *Spitzer* Extragalactic Representative Volume Survey (SERVS; Lacy et al., in preparation) and *Herschel* Multi-tiered Extragalactic Survey (HerMES; Oliver et al., in preparation) as demonstrated in recent publications (e.g. Eales et al. 2010; Hatziminaoglou et al. 2010; Roseboom et al. 2010; Rowan-Robinson et al. 2010; Vaccari et al. 2010).

Section 2 summarizes the observations and general properties of the data; the data processing is described in Section 3. Photometric calibration is performed using the SDSS, and the colour equations are provided in Section 4. Catalogues are described in Section 5; these have been matched to the UKIDSS and SWIRE data where available, and the process is described in Section 6 together with an example estimation of photometric redshifts.

Images, cut-outs and catalogues are publicly available from the Cambridge Astronomy Survey Unit (CASU) web pages.[1] Additionally, catalogues are also available through ViZieR.

2 OBSERVATIONS

Observations have been made using the WFC on the 2.5-m INT on the Observatorio del Roque de Los Muchachos, La Palma. The INT WFC consists of four 2048 × 4096 pixel CCDs, covering a field of view of 0.29 deg^2 with a pixel scale of 0.33 arcsec. The camera CCD detectors are configured in an L shape and CCD number 3 is slightly vignetted in one corner. There is a small gap between detectors which leaves about 2 per cent of the total field of view uncovered. In these observations we have not attempted to do offsets to cover the chip gaps. The broad-band filters are slightly different to the SDSS filters resulting in the need to introduce colour equations to transform between both. In particular, the WFC filters are slightly redder than their counterparts in SDSS as shown in Fig. 2 where the quantum efficiency (QE) of the detectors has also been taken into account.

[1] http://casu.ast.cam.ac.uk

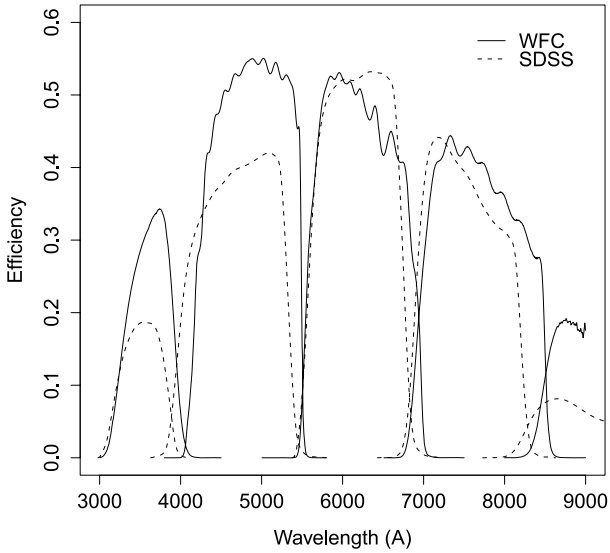

Figure 2. Efficiency curves of the *ugriz* filters from the WFC (continuous line) and from SDSS (dashed line).

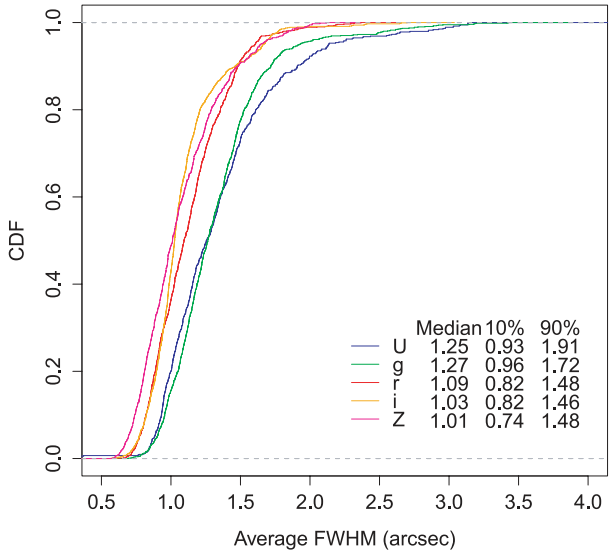

Figure 3. Seeing distribution per band of all frames. The median and the first and ninth deciles are shown.

In ELAIS N1 (EN1) and Lockman Hole existing publicly available imaging data by the WFS and SWIRE have been extended with newer data and all the existing data recalibrated to the same photometric reference producing homogeneous data products over all the fields. Catalogues have been re-extracted to contain a larger number of aperture sizes as well as different fluxes for extended objects (see Section 3.3.2). The cataloguing software has been used to produce catalogues from UKIDSS and VISTA imaging and will be used for several of the VST surveys. It has also been used to carry out object extraction and produce catalogues for a wide range of imaging data, including SuprimeCam, MegaCam, Mosaic and WFI, and it is available, together with stacking, mosaicking, astrometry and classification software from the CASU web site.

Images were obtained in several runs on semesters 99A, 99B, 00A, 00B, 01A, 02A, 02B, 05A, 05B, 06A and 09A, for a total of 112 nights and nearly 900 h of integration time. Images were acquired with one exposure of 600 s in each band. We have extended these data with 100 h of g, r, i observations in the Lockman Hole done with the Mosaic 1 camera on the Mayall 4-m Telescope of Kitt Peak National Observatory (KPNO). This camera consists of eight 2048×4096 pixel CCDs, covering an area of 36×36 arcmin^2 with a pixel scale of 0.26 arcsec (Muller et al. 1998). Broad-band filters are similar to those used in the INT WFC.

Weather conditions were variable across the different observing runs with both good photometric nights and some not so good ones, but as shown below these are flagged during pipeline processing. The median seeing of the observations varies between 1 and 1.2 arcsec depending on the filter (Fig. 3).

3 DATA PROCESSING

All the observations obtained with the INT at La Palma are transmitted in pseudo-real time to the CASU for data archival via the internet. Although quasi-real time data processing is possible, it is preferable to perform the data processing on a run-by-run basis. The calibration is then performed using the whole run master flats and biases. For each observation the imaging data are stored in a multi-extension FITS (MEF) file with a primary header describing the overall characteristics of the observation (pointing, filter, exposure time, etc.) and four image extensions corresponding to each of the CCD detectors.

The data are processed by CASU as described in Irwin & Lewis (2001) following the same steps as for the processing of the WFS, which used the same telescope and camera combination. We provide here a short description of the reduction steps followed in the INT WFC data. The processing of the KPNO data follows a similar procedure. More technical information and detailed description of the algorithms used are available in Irwin (1985) and Irwin et al. (in preparation).

3.1 Removal of instrument signature

3.1.1 Bias and flat-field correction

The data are first debiased (full 2D bias removal is necessary). Bad pixels and columns are then flagged and recorded in confidence maps, which are used later during catalogue generation. Optical detectors are generally non-linear, an effect which is usually overlooked but which generally is at the levels of a few per cent. In the case of the WFC linearity tests, using sequences of dome flats revealed that the CCDs have significant non-linearities at the level of 1–2 per cent (Fig. 4) depending on the detector, the readout mode and the period of observation. Due to several changes to the WFC controllers, the linearity values change from time to time, so linearity measurements need to be updated periodically. A linearity correction using look-up tables is then applied to all data prior to any further processing. Flat-field images in each band are constructed by combining a series of sky flats obtained in bright sky conditions during the twilight for each run.

3.1.2 Confidence maps

We define a confidence c_{ij} map, where j refers to pixel j of frame i, which is an inverse variance weight map in units of relative variance denoting the confidence associated with the flux value in each pixel. The c_{ij} are normalized to a median level of 100 per cent (i.e. $\langle c_{ij} \rangle = 1$). This has the advantage that the same map can also be used to encode for hot, bad or dead pixels, by assigning zero confidence.

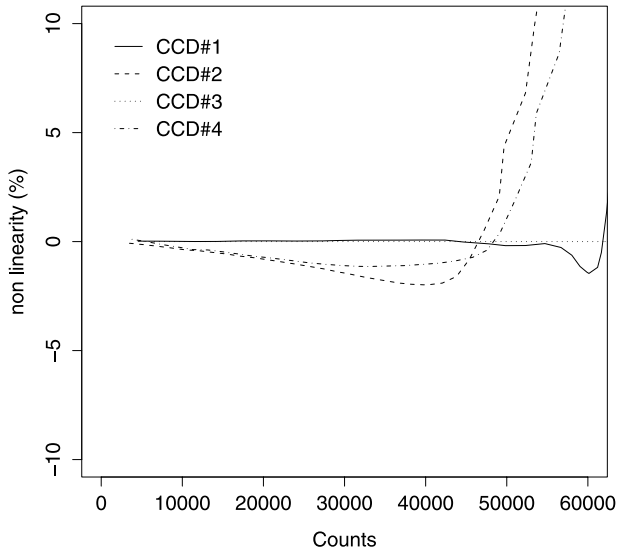

Figure 4. Non-linearity of the WFC detectors as measured in 2007 May for the 'fast' readout mode.

The confidence map for each frame is derived from an analysis of the flat-fields and is unique for each filter/detector combination. It encodes individual pixel sensitivities and allows for vignetted or bad regions to be masked.

3.1.3 Defringing

Fringing is the interference pattern caused by reflections on the inside of thin, back-illuminated CCD detectors and are important at the longer wavelengths. Both *i*- and *Z*-band data frames suffer from significant sky fringes, at a level of 2 per cent of the sky in the *i* band and 6 per cent of the sky in the *Z* band. For reference, the rms dark sky photon noise is approximately 1 per cent of the sky for a 600-s exposure. In order to remove the fringes, it is important that the sky flats have been obtained in bright sky conditions so that the effect of the fringing in them is negligible. We then construct a master fringe frame combining a sufficient number of science observations on each filter. We find that the fringe pattern is fairly constant in a run period of about a week. The fringe frame is then scaled and subtracted from each science image. After this removal, the residual fringe pattern is generally one-tenth of the original level; in particular in the *i* band the residual fringe patterns are visible at a level of the order of 0.2 per cent of the sky, and the *Z* band at a level of 0.4 per cent of the sky.

3.2 Astrometry and astrometric distortion

The astrometric solution starts with a rough World Coordinate System (WCS) based on the known telescope pointing and camera geometry and is then progressively refined using the 2MASS catalogue. The WFC field distortion (see below) is modelled using a zenithal equidistant projection with polynomial radial distortion (Greisen & Calabretta 2002). The resulting internal astrometric precision is better than 100 mas over the whole WFC array, based on the astrometric residuals derived from stacking independent WFC pointings. Fig. 5 shows the 2D and the radial residuals of the WFC positions compared to 2MASS from stacking about a hundred frames. The external astrometric accuracy is comparable to 2MASS, i.e. of the order of 0.10–0.11 arcsec as shown in Figs 6 and 7.

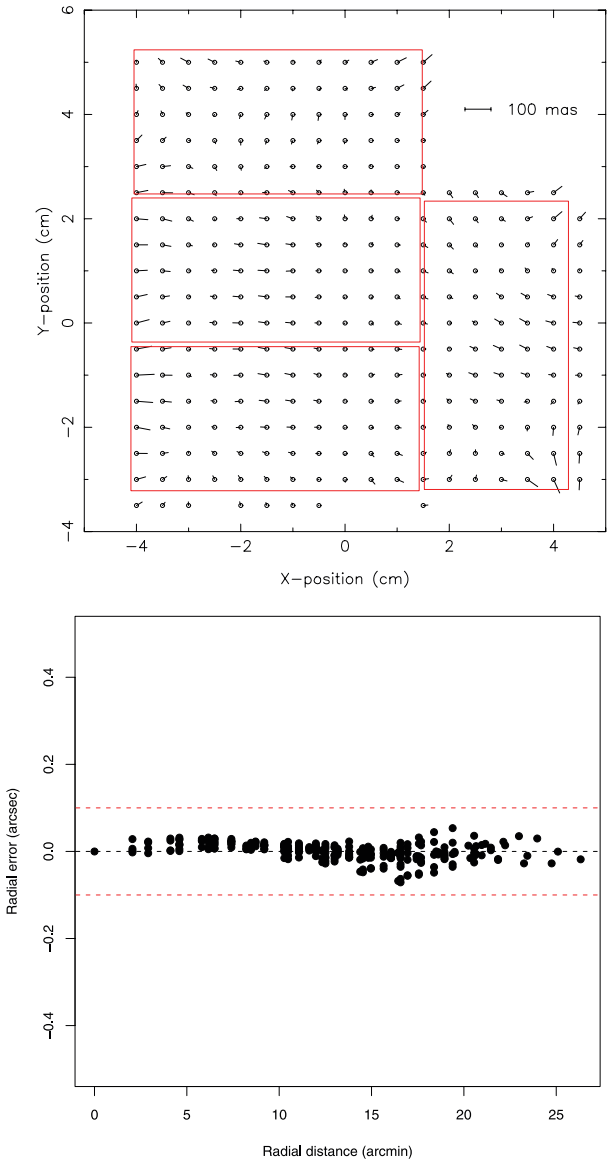

Figure 5. Top: astrometric residuals derived from a series of independent WFC pointings. The residuals are shown in physical coordinates with respect to the centre of the optical axis. Bottom: radial error versus distance from stacking analysis of all frames.

Optical systems do not have a uniform plate scale over the field and generally have a radial distortion term which can be modelled as a polynomial. In radians, the expression of the astrometric distortion for the WFC is

$$r = r' \left(1 + \frac{P_3}{P_1} r'^2\right), \quad (1)$$

where r is the true distance of an object from the optical axis as measured in the sky and r' is the measured distance. The default coefficient is $P_3/P_1 = 220.0$ and does not depend on the waveband. Unlike instruments like SuprimeCam or the VISTA Infrared Camera (VIRCAM), we find that it is not necessary to introduce a r^5 term to model the distortion.

This astrometric distortion leads to a decrease in pixel area by about 1–2 per cent compared to the centre of the field of view (Fig. 8). When we process the images, we use the flat-field to produce a flat background, but we would expect to see a decrease

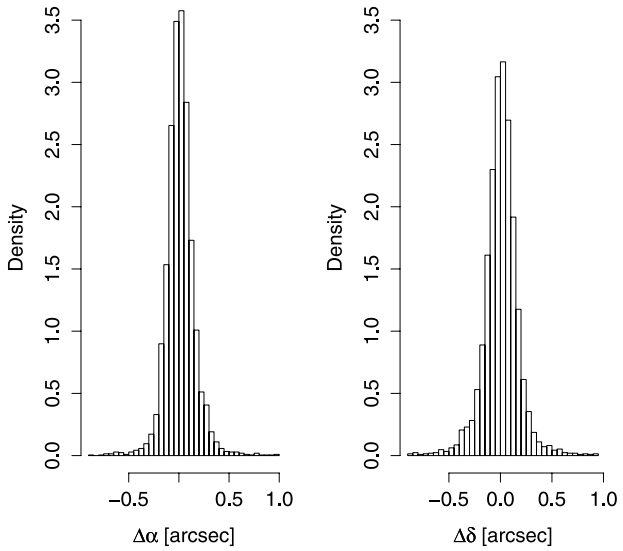

Figure 6. Differences in RA and Dec. between the 2MASS positions and the derived WFC positions. The rms in these histograms is 0.15 arcsec.

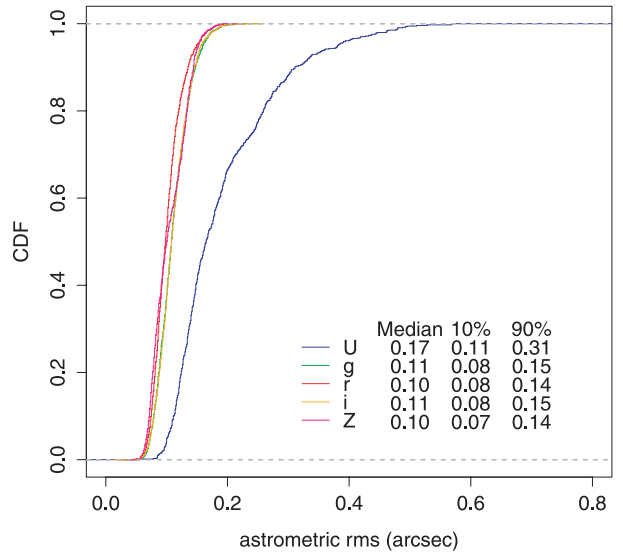

Figure 7. Cumulative density function showing the distribution of the astrometric residuals for each band in all chips; the median and the first and ninth deciles of the distribution are shown.

in the sky counts per pixel at large off-axis angles, while the total number of counts detected from a star would be independent of its position on the array. The flat-fielding of an image therefore introduces a systematic error into the photometry of sources towards the edge of the field of view.

This photometric factor is as large as 0.035 mag at the edge of the focal plane (i.e. around 20 arcsec radius, see Fig. 9), and we correct for it in the catalogue stage (see Section 3.3).

Note that we choose not to include this correction in the image by not resampling the pixel data into a tangent plane projection as many other projects do. The benefit of this approach is that we do not need to add an additional modification to the pixels, introducing systematics and correlated noise.

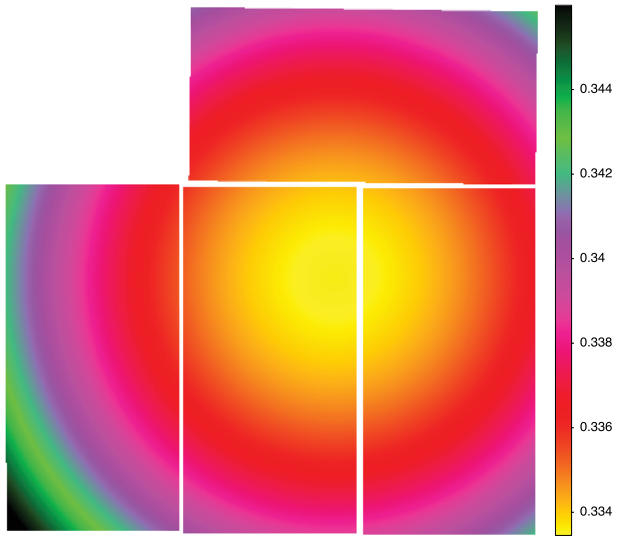

Figure 8. The projected pixel scale of the WFC varies by about 0.01 arcsec from the centre to the edge.

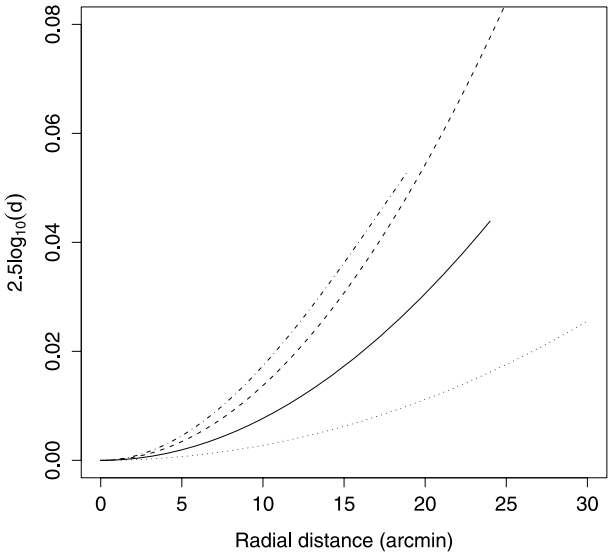

Figure 9. Effect of scale change in photometry (magnitude versus distance to field centre) for the WFC (continuous line) and KPNO/Mosaic (dashed line). For comparison we plot the distortion effect for MegaCam (dotted line) and SuprimeCam (dot–dashed line).

3.3 Catalogue extraction

The catalogue generation is carried out by IMCORE[2] (Irwin 1985) and makes direct use of the confidence maps previously generated for a variety of tasks. These include object detection and parametrization, producing quality control information, standard object descriptors and detected object overlay files. The possibly varying sky background is estimated automatically, prior to object detection, using a combination of robust iteratively clipped estimators. The image catalogues are then further processed to yield morphological classification for detected objects and used to generate astrometric and photometric calibration information.

[2] Publicly available from http://casu.ast.cam.ac.uk.

Each detected object has an attached set of descriptors, forming the columns of the binary table and summarizing derived position, shape and intensity information. During further processing stages, ancillary information such as the sky properties, seeing and mean stellar image ellipticity are derived from the catalogues and stored in the FITS headers attached to each catalogue extension. In addition to being the primary astronomical products from the pipeline processing, the catalogues and associated derived summary information form the basis for astrometric and photometric calibration and quality control monitoring.

3.3.1 Aperture photometry

The smaller photometric errors for point-like objects are obtained with relatively small apertures. This is because large apertures are affected by the increase of the number of photons from the sky background in the aperture (Newberry 1991; Howell 1992; Merline & Howell 1995). Too small apertures, however, can produce large photometric errors if not enough photons are recorded, so that the error is dominated by small number statistics; furthermore errors in the calculated centre of the star will also be larger if not enough point spread function (PSF) is sampled.

For a Gaussian model of the PSF, the optimum signal-to-noise ratio is obtained for a circular aperture of 0.68 full width at half-maximum (FWHM) and contains about 70 per cent of the total flux of the point-like object. For a Moffat profile with $\beta = 2.5$, the radius of the optimal aperture is 0.8 FWHM which contains about 60 per cent of the total flux (Fig. 10). Brighter stars have larger optimal aperture radius than fainter stars, but the signal-to-noise ratio is fairly insensitive to variations of the aperture size near the optical radius.

An aperture radius of FWHM makes an excellent practical compromise between concerns about systematic centring errors and diminishing signal-to-noise ratios typically obtained with larger aperture radii.

The object detection is performed in each band separately using a standard automatic plate measuring (APM) -style object detection and parametrization algorithm (Irwin 1985). The curve of growth, defined as the flux inside an aperture as a function of its radius, is calculated measuring the flux in a set of 13 soft-edged apertures of radii $r/2, r/\sqrt{2}, r, \sqrt{2}r, 2\sqrt{2}r, 2r, 4r, 5r, 6r, 7r, 8r, 10r, 12r$, where $r = 3.5$ pixels (1.2 arcsec). A soft-edged aperture divides the flux in pixels lying across the aperture boundary in proportion to the pixel area enclosed. We use the same aperture radius for all images in all filters.

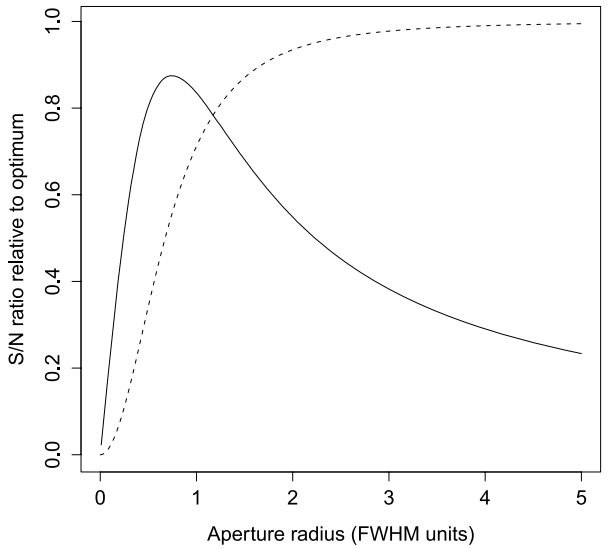

Figure 10. Signal-to-noise ratio as a function of aperture radius for a Moffat profile with $\beta = 2.5$. The dashed line represents the curve of growth. The maximum of the signal-to-noise ratio is at a radius of 0.8 FWHM and from the curve of growth it encloses about 60 per cent of the total flux. Aperture corrections are at the level of 0.56 mag for an aperture of radius 0.8 FWHM and 0.37 mag for an aperture of radius equal to the FWHM.

By using all these aperture fluxes, we compute the average curve of growth for all isolated bright stars, and we determine the aperture correction per detector to be applied to the aperture fluxes to account for the light lost outside the aperture.

A by-product of the curve-of-growth analysis and the classification is an estimate of the average PSF aperture correction for each detector for those apertures (up to and including $4r$, which includes typically ∼99 per cent, or more, of the total stellar flux) used in deriving the classification statistic. Accurate assessment of the aperture correction to place the (stellar) fluxes on a total flux scale is a crucial component of the overall calibration. We find that this method of deriving aperture corrections contributes $\leq \pm 1$ per cent to the overall photometry error budget and also provides a useful first-order seeing correction for non-stellar sources.

After dealing with overlapping objects by using multiple isophotes to correctly calculate the fluxes of the objects in the most crowded regions, we find that there is little to be gained from PSF fitting on these high-latitude fields.

Finally, a distortion correction is applied to the photometry to take into account the change of pixel scale with respect to the optical axis distance. The magnitude of the multiplicative correction to be applied to the measured flux can be modelled as (Irwin et al., in preparation)

$$d = \left(1 + \frac{3\,P_3\,r^2}{P_1}\right)\left(1 + \frac{P_3\,r^2}{P_1}\right), \qquad (2)$$

where R is the distance from the optical axis. We have remeasured the distortion coefficients for the recent WFC data, and the coefficients are $P_1 = 1$, $P_3 = 220$ (corresponding to the PV2_1 and PV2_3 WCS keywords as defined in Greisen & Calabretta 2002). For the WFC the correction is generally at the level of 2 per cent in the outer parts of the frames, while for Mosaic 1 it is about 8 per cent maximum.

3.3.2 Extended photometry

In addition to aperture fluxes, we compute Petrosian, Kron, isophotal and half-light fluxes for extended objects. We adopt the Petrosian radius, $r_{\rm P}$, as defined in Yasuda et al. (2001) and calculate the Petrosian flux as the flux within a circular aperture of radius $2r_{\rm P}$. The Kron radius, $r_{\rm K}$, is calculated as described in Bertin & Arnouts (1996), and the Kron flux is defined as the flux within the circular aperture of radius $2r_{\rm K}$.

Note that $r_{\rm P}$ and $r_{\rm K}$ are defined independently in each of the bands. However, the curve of growth defined by 13 aperture sizes allows us to calculate the flux in any radius, so one can define the Petrosian or Kron radius in the r band and calculate the flux within that radius in any of the other bands by interpolation.

Fig. 11 shows the various apertures defined for a set of different objects. The Petrosian radius is generally larger than the Kron radius, and it is usually the best measurement of the total flux from a galaxy. The drawback is that larger apertures also mean larger flux errors.

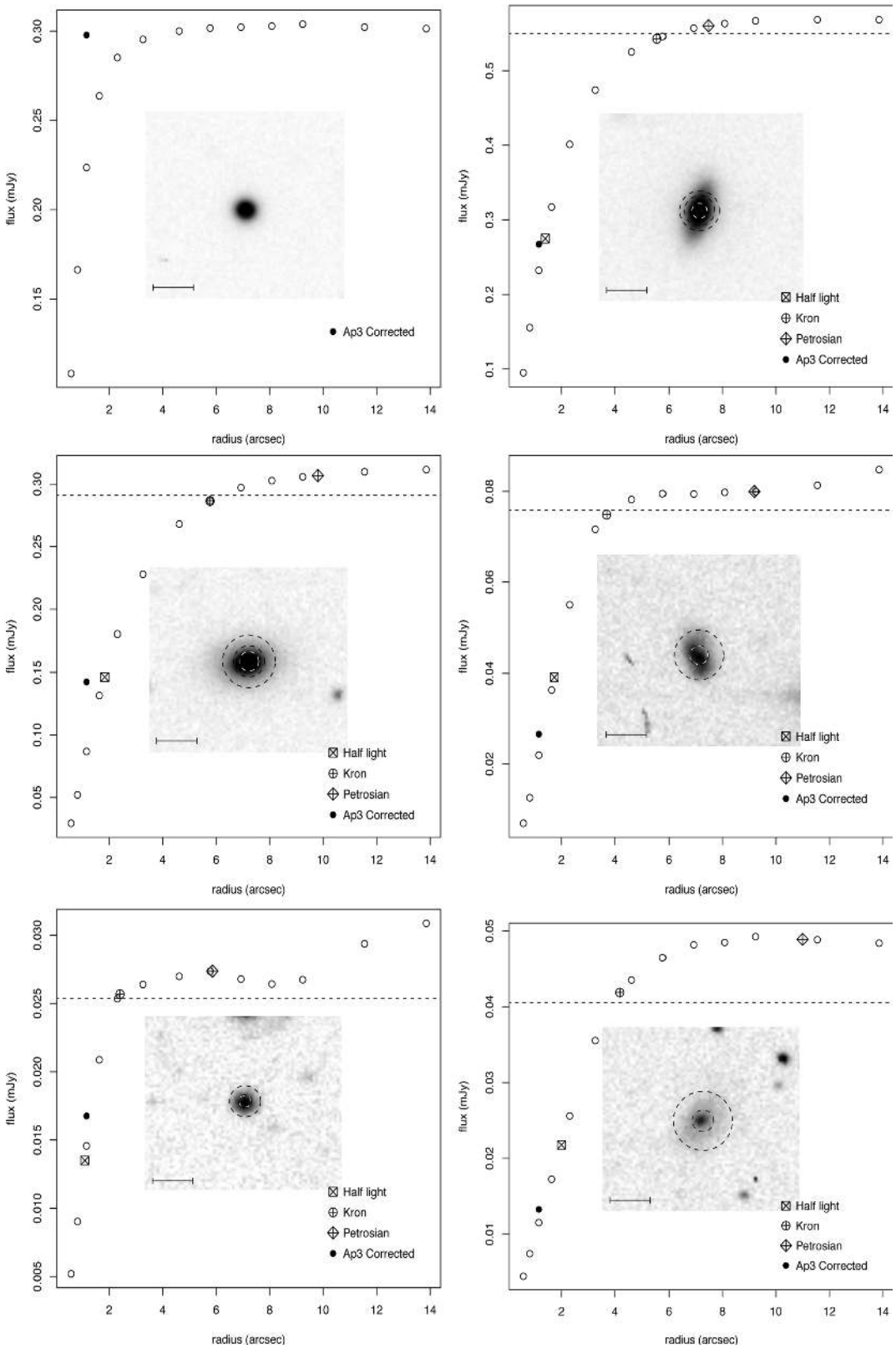

Figure 11. Curve of growth for different objects. Each open dot shows the flux measured in the corresponding aperture radius (not aperture corrected), while the filled dot shows the corrected aperture magnitude in the default aperture. The top-left panel shows a relative bright star, for which the corrected aperture magnitude represents well the total magnitude. The rest of the figures show galaxies of different brightness, showing as well the Kron and Petrosian fluxes and radius. The dashed line shows the location of the isophotal flux. The *x*- and *y*-axes refer to the curve of growth, while the bar in the bottom left of each inset image represents 10 arcsec in the background image.

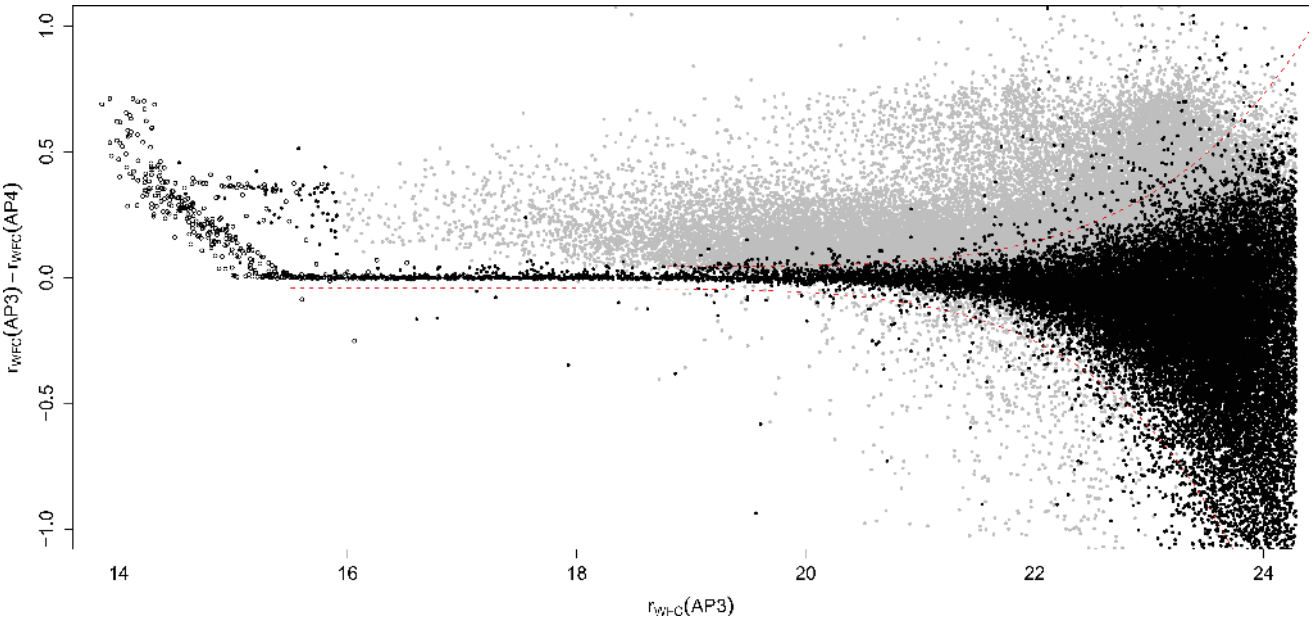

Figure 12. Difference between aperture magnitudes (once aperture corrected) versus aperture magnitude for extended objects (grey) and point-like objects (filled black). Open circles represent objects classified as saturated. The dashed lines enclose the stellar locus defined as the expected 3σ magnitude error for a point-like object measured in the default aperture. We use the information from all apertures to finally derive a stellar classification statistic.

3.3.3 Confusion

In order to determine the effect of possible crowding of our images in our detection, we use the nearest neighbour probability density distribution (PDF) expected for a random sample which can be written as (Bahcall & Soneira 1981)

$$P_{\rm NN}(\theta) = 2\pi\,\rho\,\theta\,{\rm e}^{-\pi\rho\theta^2}, \tag{3}$$

where ρ is the average density and $\pi\rho\theta^2$ is the expected number of neighbours in the interval $(0, \theta)$. The expected mean nearest neighbour separation can then be calculated as (Scott & Tout 1989)

$$\langle\,\theta\,\rangle = \int_0^\infty \theta\; P_{\rm NN}(\theta)\,{\rm d}\theta = \frac{1}{2\sqrt{\rho}}. \tag{4}$$

For the space densities typical of our fields, we obtain $\langle\,\theta\,\rangle = 8.5$ arcsec. More meaningful is the most probable neighbour separation given by $\theta_{\rm nn} = 1/\sqrt{2\pi\rho} = 6.8$ arcsec. We can determine the fraction of missed objects due to crowding by calculating the probability that given a source there is another one within the FWHM of the image, plus the probability that there is a third one within that limit, and so on. Integrating over all the possibilities, we arrive at the following expression (Irwin & Trimble 1984):

$$\rho_{\rm corr} = -\frac{\log(1 - 4\pi\rho\,\theta^2_{\rm FWHM})}{4\pi\,\theta^2_{\rm FWHM}}, \tag{5}$$

where $\rho_{\rm corr}$ is the corrected average density and $\theta_{\rm FWHM}$ is the FWHM of the images. For our images, this ranges from 0.6 to 0.1 per cent, i.e. negligible for most of the studies.

3.4 Morphological classification

The morphological classification is based primarily on the aperture fluxes and the discrete curve of growth for each detected object defined by them. Ancillary information such as object ellipticity derived from intensity-weighted second moments is also used but only as a secondary indicator. The curve of growth is a direct measure of the integral of the PSF out to various radii and is independent of magnitude if the data are properly linearized, and if saturated images are excluded. In using this property, the classifier further assumes that the effective PSF for stellar objects is constant over each detector. In practice, we find that the effects of the spatial variation of the PSF on the aperture fluxes at the detector level are generally negligible. Individual detectors are allowed to have different PSFs since all detectors, pointings and passbands are treated independently.

In practice, the aperture with radius $r = 1.2$ arcsec is used as a fixed reference and also defines the internal magnitude (flux) scale. The linearity of the system implies that the position of the stellar locus for *any function* of the aperture fluxes is independent of magnitude (at least until images saturate). Therefore marginalizing the flux ratios over magnitude yields 1D distributions that can be used to greatly simplify locating the stellar locus using an iteratively clipped median. With the location estimated, the median of the absolute deviation from the median provides a robust measure of the scatter about this locus as a function of magnitude, at least until galaxies dominate in number (Fig. 12). This process is repeated iteratively for each distribution, using 3σ clipping to remove non-stellar outliers, until satisfactory convergence is reached. We also calculate a saturation level for each chip, based on the information from all the apertures and defined as the flux where the difference between the several aperture fluxes for bright objects is larger that 3σ the expected error. For an object to be classified as saturated, we choose a conservative approach that its peak flux plus the sky level is greater than 90 per cent of the saturation limit.

4 PHOTOMETRIC CALIBRATION

Calibration of photometric nights is done using series of Landolt standard stars (Landolt 1992) with photometry in the SDSS system with additional stars from Stetson (2000). For each night, a zero-point and error estimate using the observations of all the standard

fields in each filter is derived. The calibration over the whole mosaic has an accuracy of 1–2 per cent. All calibration is by default corrected during pipeline processing for the mean atmospheric extinction at La Palma (0.46 in u, 0.19 in g, 0.09 in r, 0.05 in i and 0.05 in z per unit airmass).

Next we derive the colour equations between the WFC and SDSS system. Using Data Release 7 (DR7), we match the position of all point-like objects (as classified in the WFC images) using the nearest neighbour within a radius of 1 arcsec. For each chip, we independently fit a transformation as follows:

$$u_{\rm WFC} = u_{\rm SDSS} + A_u + B_u\,(u_{\rm SDSS} - g_{\rm SDSS}),$$
$$g_{\rm WFC} = g_{\rm SDSS} + A_g + B_g\,(g_{\rm SDSS} - r_{\rm SDSS}),$$
$$r_{\rm WFC} = r_{\rm SDSS} + A_r + B_r\,(g_{\rm SDSS} - r_{\rm SDSS}),$$
$$i_{\rm WFC} = i_{\rm SDSS} + A_i + B_i\,(r_{\rm SDSS} - i_{\rm SDSS}),$$
$$z_{\rm WFC} = z_{\rm SDSS} + A_z + B_z\,(i_{\rm SDSS} - z_{\rm SDSS}),$$

where A_x is the offset between both systems and B_x is the colour term. We use PSF magnitudes for SDSS and aperture-corrected magnitudes with an aperture size selected to match the seeing of the image for the WFC. The difference between the fits for different chips is negligible in the final photometry (∼0.1 per cent), so we decided to use one set of equations for all chips. The results in each band are shown in Fig. 13 and are given by the following equations:

$$u_{\rm WFC}[{\rm Vega}] = u_{\rm SDSS} - 0.833 - 0.009\,(u_{\rm SDSS} - g_{\rm SDSS}),$$
$$g_{\rm WFC}[{\rm Vega}] = g_{\rm SDSS} + 0.060 - 0.136\,(g_{\rm SDSS} - r_{\rm SDSS}),$$
$$r_{\rm WFC}[{\rm Vega}] = r_{\rm SDSS} - 0.144 + 0.006\,(g_{\rm SDSS} - r_{\rm SDSS}),$$
$$i_{\rm WFC}[{\rm Vega}] = i_{\rm SDSS} - 0.411 - 0.073\,(r_{\rm SDSS} - i_{\rm SDSS}),$$
$$z_{\rm WFC}[{\rm Vega}] = z_{\rm SDSS} - 0.525 - 0.013\,(i_{\rm SDSS} - z_{\rm SDSS}),$$

$$u_{\rm WFC}[AB] = u_{\rm SDSS} + 0.010 - 0.009\,(u_{\rm SDSS} - g_{\rm SDSS}),$$
$$g_{\rm WFC}[AB] = g_{\rm SDSS} - 0.035 - 0.136\,(g_{\rm SDSS} - r_{\rm SDSS}),$$
$$r_{\rm WFC}[AB] = r_{\rm SDSS} + 0.002 + 0.006\,(g_{\rm SDSS} - r_{\rm SDSS}),$$
$$i_{\rm WFC}[AB] = i_{\rm SDSS} - 0.017 - 0.073\,(r_{\rm SDSS} - i_{\rm SDSS}),$$
$$z_{\rm WFC}[AB] = z_{\rm SDSS} - 0.002 - 0.013\,(i_{\rm SDSS} - z_{\rm SDSS}),$$

where A_x and B_x had been derived by averaging the values obtained from the fits in each chip. The independent term has been fixed so that the magnitudes of Vega on the INT WFC and SDSS data agree (Fukugita et al. 1996). This gives the following magnitudes for Vega: $u_{\rm WFC}[{\rm Vega}] = 0.138$, $g_{\rm WFC}[{\rm Vega}] = 0.002$, $r_{\rm WFC}[{\rm Vega}] = 0.020$, $i_{\rm WFC}[{\rm Vega}] = 0.003$ and $z_{\rm WFC}[{\rm Vega}] = 0.050$. The transformations from AB to Vega used for each passband are 0.843, −0.095, 0.146, 0.394 and 0.523, respectively, computed using the Vega spectrum from Bohlin & Gilliland (2004).

We use these transformations to derive a zero-point for each image, but we do not take into account the independent term A_x so the WFC magnitudes are calibrated using SDSS given in AB in the natural WFC system. Zero-points are used to derive magnitudes for each source in the following way:

$$m = {\rm ZP} + m_{\rm inst} - \kappa(X - 1) - a - 2.5\log 10(d),$$

where ZP is derived zero-point at unit airmass, $m_{\rm inst} = -2.5\log 10({\rm count\,exptime}^{-1})$ is the instrumental magnitude, κ is the default extinction coefficient for a photometric night, X is the airmass, a is the aperture correction and d is the distortion correction. Note that the zero-point is only a function of the instrument (including telescope and optics). Our definition, however, includes the contribution of the real extinction for each particular observation. The derived values defined in this way can then be used to

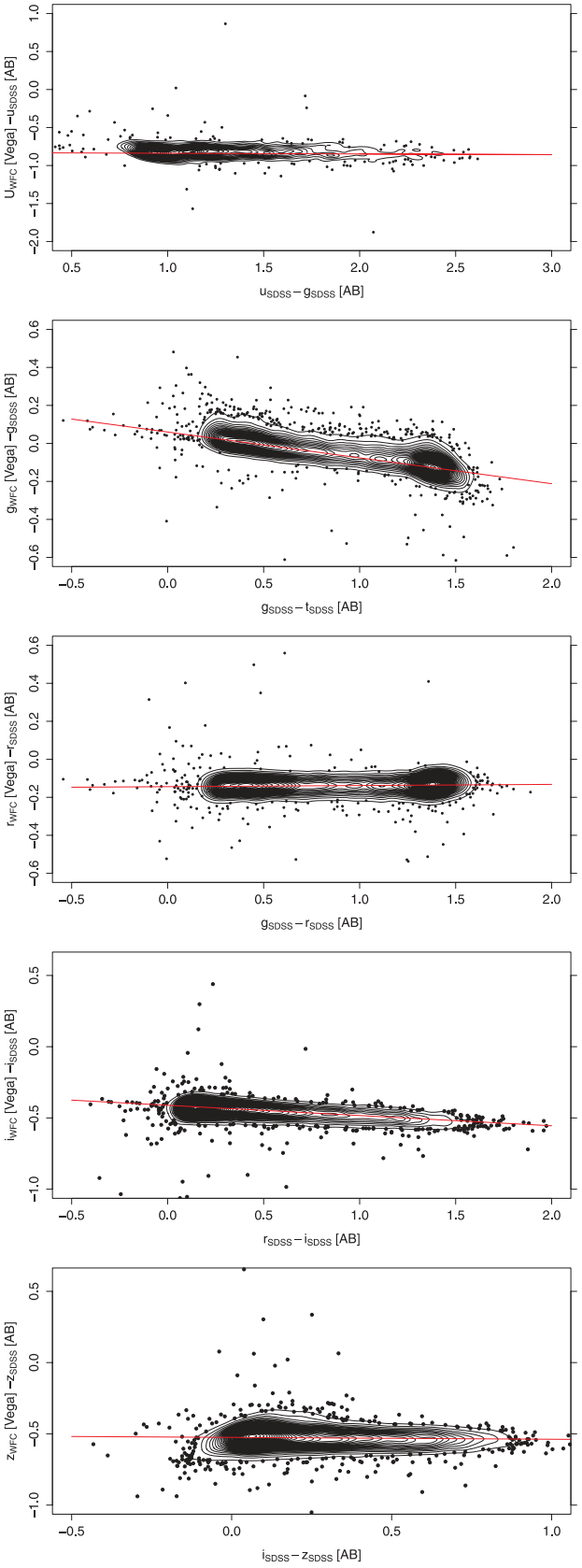

Figure 13. WFC versus SDSS colours and fits used to derive the photometric transformations between both systems. Object density is plotted as contours.

monitor the photometric quality of data for each particular observation.

4.1 Repeatability of the photometry

In order to investigate the internal accuracy of the photometry, we can use the repeat observations in the overlap areas between adjacent pointings (we allow for a 10 per cent overlap in the observations). Note that by comparing multiple observations of sources near the edges of the detectors we are more sensitive to systematics from spatial effects, so this analysis should demonstrate the worst case scenario. Fig. 14 shows the rms for the repeat observations in each band for all point sources calculated as the difference of the magnitudes determined in two different observations. At the bright end, the rms is very close to 0.01 in the g, r and i bands, and increases to 0.02 in the z band and 0.03 in the u band. The random noise errors estimated by the pipeline (Fig. 15) are thus underpredicted, as expected, by a factor of 1–2 per cent at the bright end, indicating that systematic errors dominate in this regime (see Hodgkin et al. 2009).

5 BAND MERGE AND CATALOGUE CREATION

All image catalogues are first merged into a single catalogue per band. Duplicate sources arising from overlaps and areas observed more than twice are dealt with by selecting objects within a 1.0-arcsec distance of each other and keeping only one of them, selecting the best one based on the signal-to-noise ratio and proximity to any of the chip edges.

A band-merged catalogue is then produced by cross-matching the different bands within a search radius of 1.2 arcsec in order to minimize the number of false matches and keeping the nearest match.

5.1 Catalogue contents

The catalogue is divided into two tables, one containing the image-derived parameters extracted from the images and another containing data quality control values, observation parameters and aperture corrections. The contents of the catalogue is summarized in Tables 1 and 2.

Aperture-corrected magnitudes are given in 13 different aperture sizes, with the minimum being 0.6 arcsec and the maximum being 15.6 arcsec. This defines the curve of growth which can be used to derive the aperture magnitude for any aperture size between these two by interpolation. Note that in order to do this, one needs the aperture corrections used which are also provided in the quality control catalogue for apertures 1–7 since for larger apertures the correction is null for point sources.

Fig. 16 shows a colour–colour diagram for point-like objects detected in the First Look Survey (FLS) field. Fig. 17 shows a comparison between SDSS and WFC magnitudes, demonstrating their good agreement.

In addition to aperture-corrected magnitude, the catalogue software also provides quantities which may be more appropriate for extended objects. These include Petrosian (Yasuda et al. 2001), Kron (Bertin & Arnouts 1996) and half-light magnitudes and radius.

For each band, we also provide one individual star/galaxy classification flag (?class) which takes a discrete value according to the following key: saturated $= -9$, probable point-like $= -2$, point-like $= -1$, noise $= 0$ and extended $= 1$. All these individual flags are combined into a merged probability of the object been point-like

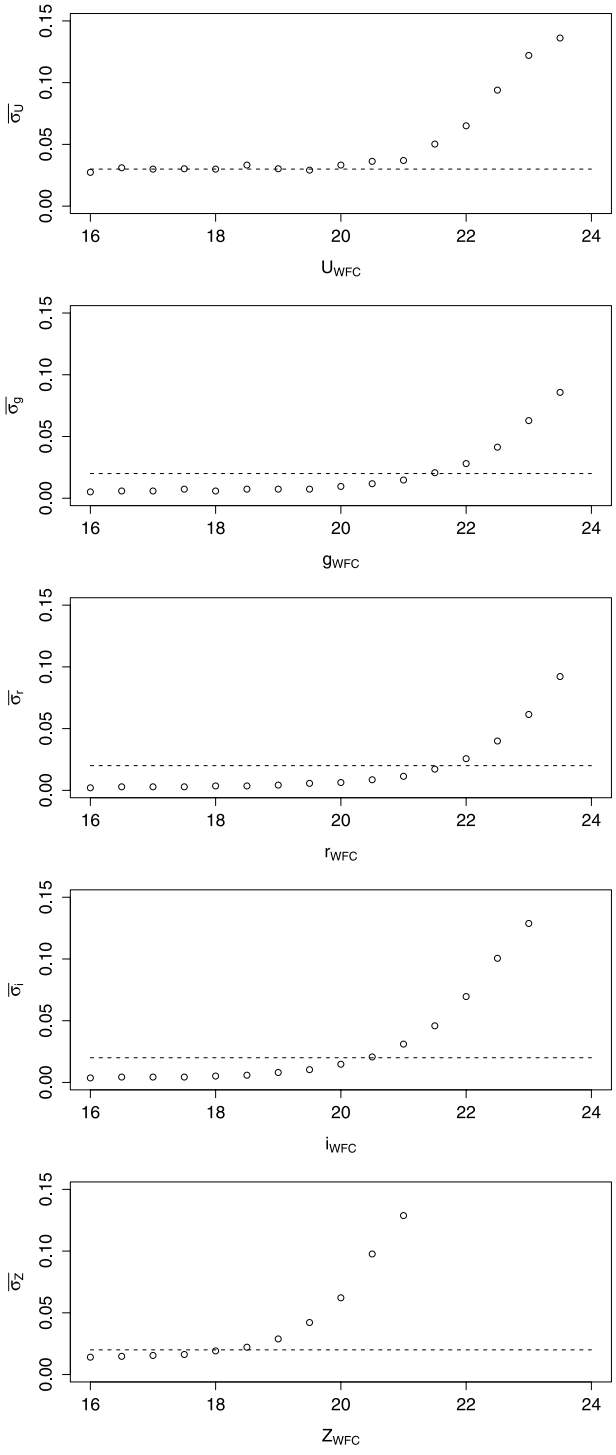

Figure 14. The rms diagram for repeat observations of stellar sources. Each symbol represents 1.48 times the median absolute deviation (MAD) of the data in magnitude slices. The dashed line is at rms of 0.02 for all bands except for U band, in which it is at 0.03.

or extended (pstar and pgalaxy) using Bayesian classification rules assuming each value is independent using the following equation:

$$P(c_k) = \prod_j P(c_k)_j / \sum_k \prod_j P(c_k)_j,$$

where c_k is the classification flag, $P(c_k)$ is the probability assigned to the classification flag c_k given in Table 3 and i denotes the ith

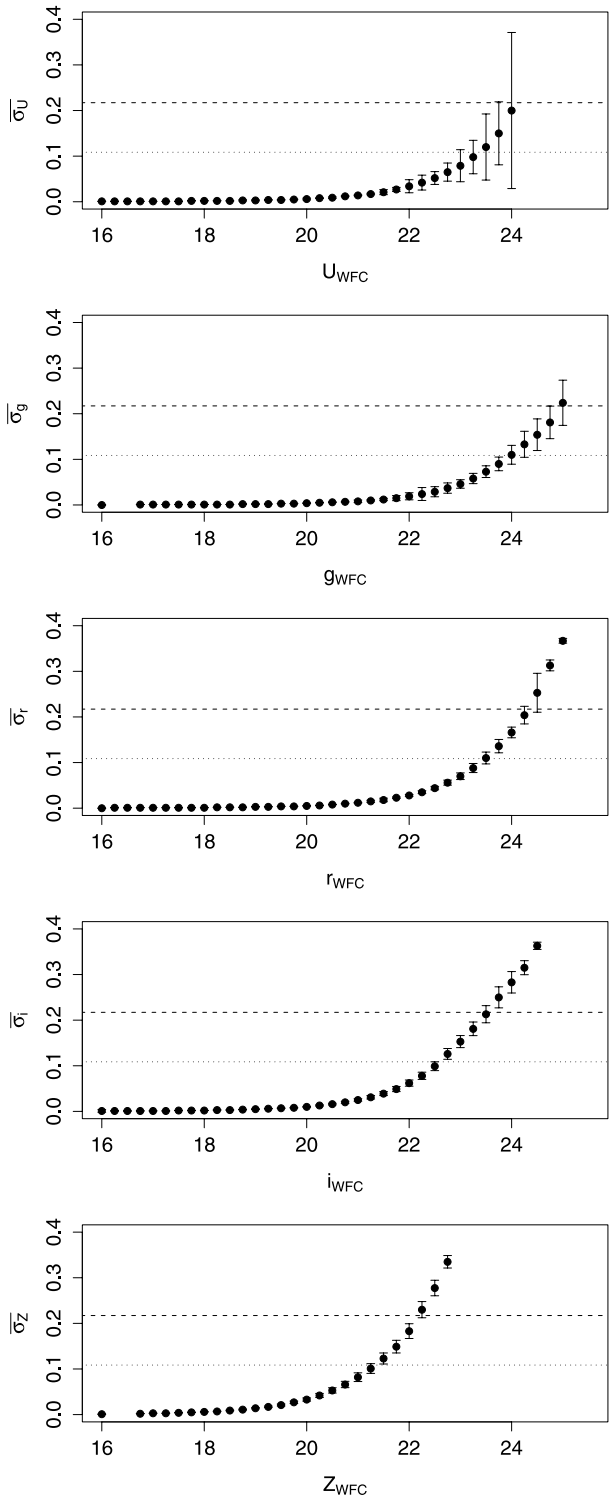

Figure 15. Average magnitude measurement uncertainties in 0.25 mag bins as a function of magnitude. The vertical error bars show the rms dispersion in the mean uncertainties in each bin, and the horizontal lines show the 5σ (dashed) and 10σ (dotted) levels.

single-detection passband measurement available. Decision thresholds for the resulting discrete classification flag are 90 per cent for definitive and 70 per cent for probable. When any of the individual classification flags denotes saturation, the probability is assigned a value of 255.

Table 1. Optical catalogue contents.

Name	Description	Units
id	Object ID	
ra	RA (J2000)	°
decl	Dec. (J2000)	°
coords	Coordinates in sexagesimal format	
	...begin for each band in order *rgizu*...	
rid	Object ID of *r*-band detection	
rmag[1-13]	*r*-band aperture-corrected magnitude	AB
remag[1-13]	*r*-band magnitude error	AB
rkronmag	*r* Kron magnitude	AB
rekronmag	*r* Kron magnitude error	AB
rkronrad	*r* Kron radius	arcsec
rhalfmag	*r* half-light magnitude	AB
rehalfmag	*r* half-light magnitude error	AB
rhalfrad	*r* half-light radius	arcsec
rpetromag	*r* Petrosian magnitude	AB
repetromag	*r* Petrosian magnitude error	AB
rpetrorad	*r* Petrosian radius	arcsec
risomag	*r* isophotal magnitude	AB
reisomag	*r* isophotal magnitude error	AB
rclass	*r*-band star/galaxy classification	
rgauss	*r* Gaussian σ of source profile	arcsec
rellip	*r* ellipticity of source	
ravconf	*r* average confidence in default aperture	
rdeblend	Deblend flag	
redgeflag	Near-edge flag	
rimage_id	id of image in the QC table	
rmaglim	*r* average magnitude limit in frame	
	...end for each band...	
pstar	Combined multiband star class	
pgalaxy	Combined multiband galaxy class	
relflag	Reliability flag (see text)	

Table 2. Optical quality control catalogue contents.

Name	Description	Units
id	Image ID	
runno	Run number of observation	
ccdno	CCD number	
waveband	Band of observation	
instrument	Instrument	
mjd	MJD of observation	
dateobs	Date of observation	
exptime	Exposure time	
apcor[1-7]	Aperture correction	AB
avseeing	Average seeing of observation	arcsec
avelliptic	Average ellipticity of observation	
airmass	Airmass of observation	
maglim	Magnitude limit of observation	AB
magzpt	Magnitude zero-point of observation	AB
magzrr	Zero-point error	AB
skynoise	Sky noise	counts
threshold	Detection threshold	counts
stdcrms	rms of astrometric fit	arcsec
numbrms	Number of stars used in astrometric fit	
wcs	WCS information (multiple keywords)	

Quality control parameters include the average seeing, average ellipticity, magnitude limit, magnitude zero-point and its error of the observation in which that particular object has been detected.

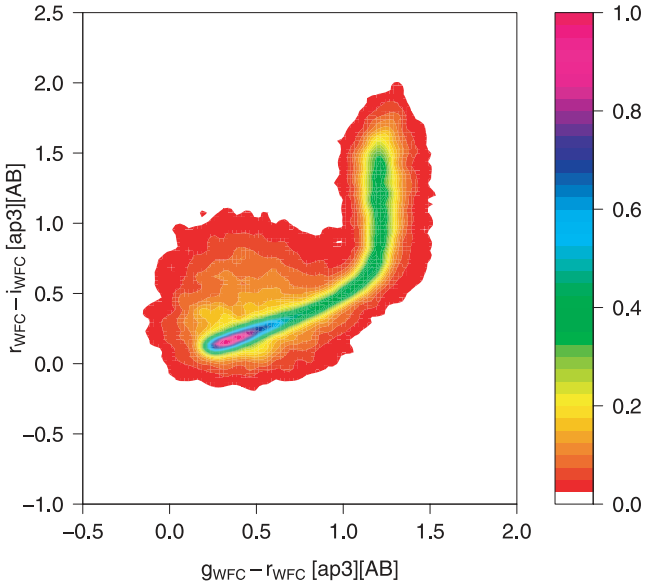

Figure 16. Colour–colour plot of all point-like objects detected in FLS. Different colours represent normalized densities according to the colour legend at the right. Note that no faint magnitude cut has been applied.

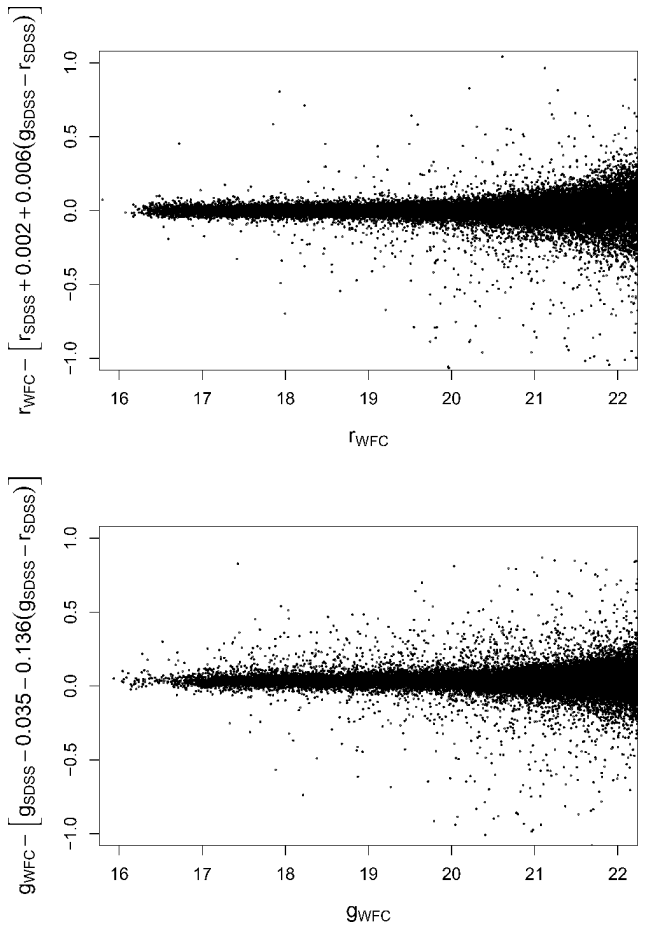

Figure 17. Comparison of SDSS and WFC *r*- and *g*-band magnitudes for point-like objects in the FLS.

Table 3. Meaning of classification index and probability assigned to each of them.

Index	Meaning	Probability (per cent)			
		Star	Extended	Noise	Saturated
−9	Saturated	0	0	5	95
−3	Probable extended	25	70	5	0
−2	Probable star	70	25	5	0
−1	Star	90	5	5	0
0	Noise	5	5	90	0
1	Extended	5	90	5	0

Objects for which there is no magnitude available lie in two categories. Either the object was not detected or the object was not observed. The ?flag parameters take the value of the magnitude limit on the former case and zero in the latter.

6 PHOTOMETRIC REDSHIFTS

As an additional assessment of the quality of photometry, we have performed photometric redshift determination using the optical WFC data, near-IR from UKIDSS and mid-IR from SWIRE in the ELAIS N1 area. Spectroscopic redshifts are taken from the literature as provided by NASA/IPAC Extragalactic Database (NED). A more comprehensive determination of photometric redshifts including these data as well as SERVS near-IR photometry will be presented in Pforr et al. (in preparation).

6.1 *J* and *K* from UKIDSS

We have cross-matched the optical catalogue with the UKIDSS DXS catalogue from DR7. The available DXS observations cover 8 deg^2 in each of the EN1 and Lockman Hole regions to a magnitude limit of *K* 22.5 (AB). Since both UKIDSS and our WFC data are astrometrically calibrated using 2MASS, no offset between the catalogues has been computed. False match ratio has been determined by offsetting the original coordinates 20 arcsec in RA and Dec., and performing the cross-match again. Fig. 18 shows the normalized number of matches versus separation in arcsec for the original

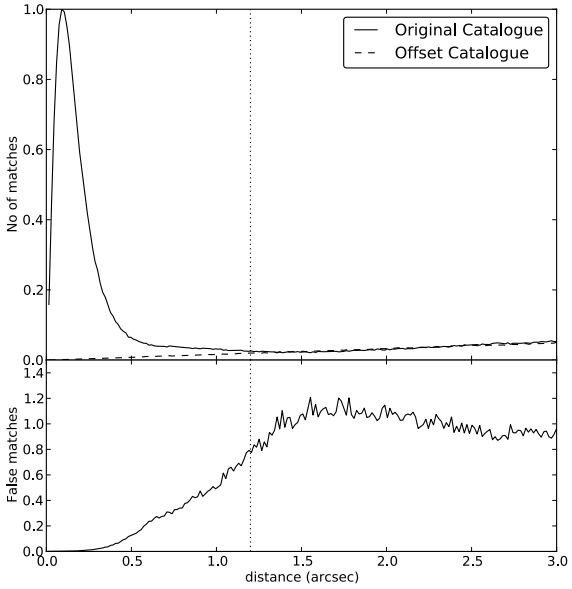

Figure 18. False match analysis between optical WFC and UKIDSS.

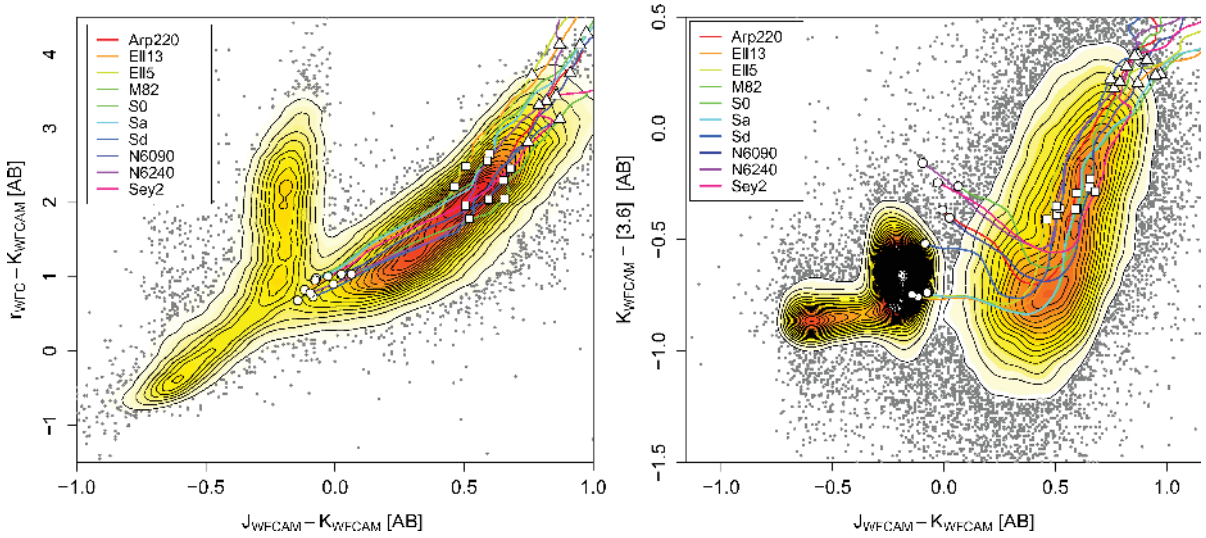

Figure 19. Colour–colour plots for the magnitudes used in the computation of photometric redshifts. Source density is shown as contours. Galaxy models used in our photometric redshift estimation are overplotted with symbols representing $z = 0$ (white dots), $z = 0.5$ (white squares) and $z = 1.0$ (white triangles).

catalogue and the offset catalogue as well as the fraction of false matches. We have chosen a value of 1.2 arcsec for the final matching radius between the two catalogues. The percentage of objects with matches in both catalogues is 60 per cent. The percentage of false matches obtained by considering the total number of matches within a distance of 1.2 arcsec over the number of false matches within the same distance is 4.9 per cent. Applying the appropriate correction factor, i.e. $(N - M)/(N - F)$, where N is the total number of sources, M the number of matches and F the number of false matches, we obtain a final false match of 2.1 per cent.

In order not to duplicate catalogues, we do not provide the full contents of the DXS DR7 catalogues but the object identification number of the matched source. We also provide a combined optical/near-IR stellar classification. The full UKIDSS catalogue can be obtained from WFCAM Science Archive (Hambly et al. 2008).

6.2 *Spitzer* SWIRE catalogues

We have used the publicly available SWIRE catalogues,[3] which contain photometry at 3.6, 4.5, 5.6 and 8.0 μm (we have not used 24-μm photometry here). These catalogues have a 60 per cent overlap with optical and 80 per cent with near-IR.

6.3 Template fitting and photometric redshifts

Care has to be taken in choosing appropriate magnitudes. For the optical and near-IR we use uncorrected aperture magnitudes measured in 2 arcsec diameter, and we compute an aperture correction for each object based on the difference between the Petrosian and the uncorrected aperture magnitude in the K band. For IRAC, we use the aperture-corrected magnitude measured in 2 arcsec diameter without further corrections. We exclude objects which are classified as point-like in any of the g, r and J bands and any object which has another one closer than 10 arcsec. We also limit ourselves at those objects with spectroscopic redshift smaller than $z = 0.8$ and detected in six or more photometric bands. This gives us a list of 456 objects with spectroscopic redshifts. We use a list of 10 templates from Polletta et al. 2007 to carry out a simple fitting to the photometric points. The templates used are three of starburst galaxies (Arp220, M82 and NGC 6090), three of spiral galaxies (S0, Sa and Sd), two ellipticals (of 5 and 13 Gyr) and two active galactic nuclei (Seyfert 2 and NGC 6240). We check that our models are a fair representation of the data by means of colour–colour plots (Fig. 19) so we do not need to apply offsets to the global calibration of the data.

We use the BPZ code (Benítez 2000) to calculate photometric redshifts using a prior based on a simple redshift distribution centred at $z \sim 0.5$ in order to take into account the degeneracy with high-redshift solutions and the low probability of finding high-redshift objects. We then use the ODDS output parameter (which basically measures the goodness of the fit taking into account the fit with the largest χ^2 and the prior) to discard those photometric redshifts with ODDS $<$ 0.95. Outliers are then inspected on the images; several of them lie near very bright stars, star spikes or close to the chip edges; so they are removed from the output list. We discard in this way 20 per cent of the sample, with the remaining 80 per cent of the objects producing a reliable photometric redshift. The uncertainties of the final determination are given by $\Delta([z_{\rm phot} - z_{\rm spec}]/[1 + z_{\rm spec}]) = 0.04$ for all objects. Fig. 20 shows the spectroscopic versus photometric redshifts for objects detected in different number of bands.

7 SUMMARY

We present in this work the wide-field imaging products used in the optical identification and analysis of the SWIRE, SERVS and HerMES surveys obtained during 1000 h of observations and covering 80 deg^2 in different optical bands. We discuss the data processing algorithms and the characteristics of the data in terms of photometric and astrometric calibration. The average magnitude limits are *u, g, r, i, z* of 23.9, 24.5, 24.0, 23.3, 22.0 (AB, 5σ for a point-like object measured in a 2-arcsec aperture). We describe the band merge with UKIDSS and SWIRE and give an example of photometric redshift

[3] Available from http://swire.ipac.caltech.edu/swire.

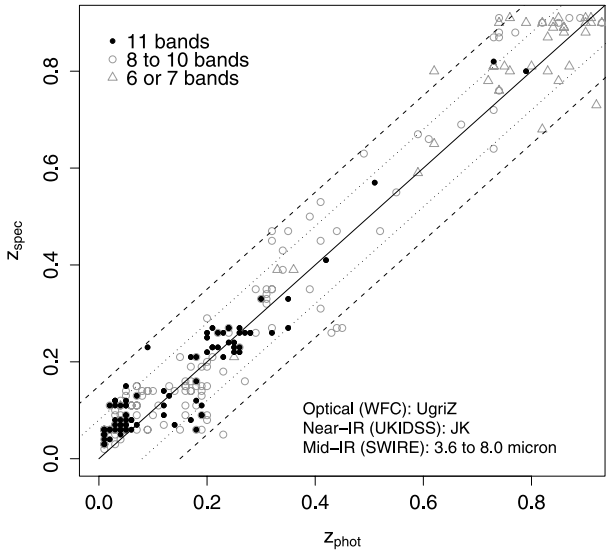

Figure 20. Photometric versus spectroscopic redshifts in the EN1 field. Different symbols represent different number of bands used. The dotted and dashed lines mark the ± 0.08 and ± 0.15 differences in redshift, respectively.

determination using the available data. Images and catalogues are publicly available from the CASU web site and ViZieR.[4]

ACKNOWLEDGMENTS

This paper makes use of data from the Isaac Newton Telescope, operated on the island of La Palma by the ING in the Spanish Observatorio del Roque de Los Muchachos of the Instituto de Astrofísica de Canarias. Archival data have been obtained from the Isaac Newton Group Archive which is maintained as part of the CASU Astronomical Data Centre at the Institute of Astronomy, Cambridge. This work is based on data products processed by the Cambridge Astronomy Survey Unit.

This research has made use of the NED which is operated by the Jet Propulsion Laboratory, California Institute of Technology, under contract with the National Aeronautics and Space Administration.

REFERENCES

Arnaboldi M., Neeser M. J., Parker L. C., Rosati P., Lombardi M., Dietrich J. P., Hummel W., 2007, Messenger, 127, 28
Bahcall J. N., Soneira R. M., 1981, ApJ, 246, 122
Benítez N., 2000, ApJ, 536, 571
Bertin E., Arnouts S., 1996, A&AS, 117, 393
Bohlin R. C., Gilliland R. L., 2004, AJ, 127, 3508
Boulade O. et al., 1998, in D'Odorico S., ed., Proc. SPIE Conf. Ser. Vol. 3355, Optical Astronomical Instrumentation. SPIE, Bellingham, p. 614
Capaccioli M., Mancini D., Sedmak G., 2002, in Tyson J. A., Wolff S., eds, Proc. SPIE Conf. Ser. Vol. 4836. SPIE, Bellingham, p. 43
Drew J. E. et al., 2005, MNRAS, 362, 753
Eales S. A. et al., 2010, A&A, 518, L23
Emerson J. P., Sutherland W. J., McPherson A. M., Craig S. C., Dalton G. B., Ward A. K., 2004, Messenger, 117, 27
Fukugita M., Ichikawa T., Gunn J. E., Doi M., Shimasaku K., Schneider D. P., 1996, AJ, 111, 1748
Gonzalez-Solares E. A. et al., 2005, MNRAS, 358, 333
Greisen E. W., Calabretta M. R., 2002, A&A, 395, 1061
Groot P. J. et al., 2009, MNRAS, 399, 323
Hambly N. C. et al., 2008, MNRAS, 384, 637
Hatziminaoglou E. et al., 2010, A&A, 518, L33
Hodgkin S. T., Irwin M. J., Hewett P. C., Warren S. J., 2009, MNRAS, 394, 675
Howell S. B., ed., 1992, ASP Conf. Ser. Vol. 23, Astronomical CCD Observing and Reduction Techniques. Astron. Soc. Pac., San Francisco, p. 345
Irwin M. J., 1985, MNRAS, 214, 575
Irwin M., Lewis J., 2001, New Astron. Rev., 45, 105
Irwin M. J., Trimble V., 1984, AJ, 89, 83
Irwin M., McMahon R., Walton N., Gonzalez-Solares E., Hodgkin S., Irwin J., Lewis J., 2005, Newslett. Isaac Newton Group Telesc., 9, 8
Iwert O. et al., 2006, in Dorn D. A., Holland A. D., eds Proc. SPIE Conf. Ser. Vol. 6276. High Energy, Optical and Infrared Detectors for Astronomy II. SPIE, Bellingham, p. 62760A
Kaiser N. et al., 2002, in Tyson J. A., Wolff S., eds, Proc. SPIE Conf. Ser. Vol. 4836. Survey and Other Telescopes Technologies and Discoveries. SPIE, Bellingham, p. 154
Landolt A. U., 1992, AJ, 104, 340
Lawrence A. et al., 2007, MNRAS, 379, 1599
Lonsdale C. J. et al., 2003, PASP, 115, 897
McMahon R. G., Walton N. A., Irwin M. J., Lewis J. R., Bunclark P. S., Jones D. H., 2001, New Astron. Rev., 45, 97
Merline W. J., Howell S. B., 1995, Exp. Astron., 6, 163
Miyazaki S. et al., 2002, PASJ, 54, 833
Muller G. P., Reed R., Armandroff T., Boroson T. A., Jacoby G. H., 1998, in D'Odorico S., ed., Proc. SPIE Conf. Ser. Vol. 3355, Optical Astronomical Instrumentation. SPIE, Bellingham, p. 577
Newberry M. V., 1991, PASP, 103, 122
Oliver S. et al., 2000, MNRAS, 316, 749
Polletta M. et al., 2007, ApJ, 663, 81
Rakich A., Blundell M., Pentland G., Brunswick R., Ferguson T., Waltho J., 2006, in Stepp L. M., ed., Proc. SPIE Conf. Ser. Vol. 6267. Ground-based and Airborne Telescopes. SPIE, Bellingham, p. 62670E
Roseboom I. G. et al., 2010, MNRAS, 409, 48
Rowan-Robinson M. et al., 2004, MNRAS, 351, 1290
Rowan-Robinson M. et al., 2008, MNRAS, 386, 697
Rowan-Robinson M. et al., 2010, MNRAS, 409, 2
Scott D., Tout C. A., 1989, MNRAS, 241, 109
Skrutskie M. F. et al., 2006, AJ, 131, 1163
Stetson P. B., 2000, PASP, 112, 925
Sweeney D. W., 2006, in Stepp L. M., ed., Proc. SPIE Conf. Ser. Vol. 6267. Ground-based and Airborne Telescopes. SPIE, Bellingham, p. 626706
Vaccari M. et al., 2010, A&A, 518, L20
Yasuda N. et al., 2001, AJ, 122, 1104
York D. G. et al., 2000, AJ, 120, 1579

[4] See http://casu.ast.cam.ac.uk/wfcdb/ for information on data access.

This paper has been typeset from a TEX/LATEX file prepared by the author.